

Cite this article as: Zheng Fanlin, Sun Tianming, Chi Hanjuan, et al. Microstructure, Corrosion Resistance, and Mechanical Properties of Biphase AlCrCoFeNi_{2.1} High Entropy Alloy Prepared by Spark Plasma Sintering[J]. Rare Metal Materials and Engineering, 2022, 51(11): 4039-4050.

ARTICLE

Microstructure, Corrosion Resistance, and Mechanical Properties of Biphase AlCrCoFeNi_{2.1} High Entropy Alloy Prepared by Spark Plasma Sintering

Zheng Fanlin¹, Sun Tianming³, Chi Hanjuan², Chen Hongsheng^{1,4}, Wang Wenxian^{3,4}

¹ College of Mechanical and Vehicle Engineering, Taiyuan University of Technology, Taiyuan 030024, China; ² Taiyuan Liuweizhai Industrial Co., Ltd, Taiyuan 030006, China; ³ College of Materials Science and Engineering, Taiyuan University of Technology, Taiyuan 030024, China; ⁴ Shanxi Key Laboratory of Advanced Magnesium-Based Materials, Taiyuan 030024, China

Abstract: The AlCrCoFeNi_{2.1} high-entropy alloy (HEA) was prepared by the spark plasma sintering method at different temperatures. The microstructure, corrosion resistance, and mechanical properties of this HEA were investigated. Results show that the maximum relative density of the AlCrCoFeNi_{2.1} HEA can reach 99.18% after sintering, and the HEA is mainly composed of body-centered cubic (bcc) and face-centered cubic (fcc) phases with the phase fraction of 20.6% and 79.4%, respectively. Compared with that in fcc phase, the fraction of recrystallized and deformed microstructures in bcc phase of AlCrCoFeNi_{2.1} HEA is higher. In addition, the bcc phase can be easily corroded in 3.5wt% NaCl solution. The pressure recovery rate of bcc and fcc phases is decreased and the hardening effect is enhanced with increasing the strain rate. The higher ultimate tensile strength of AlCrCoFeNi_{2.1} HEA after sintering at 1050 °C can be achieved due to the grain size strengthening, solid solution strengthening, and good interface bonding between HEA particles. The failure mode of AlCrCoFeNi_{2.1} HEA includes the brittle fracture of bcc phase and the ductile fracture of fcc phase.

Key words: high-entropy alloy; spark plasma sintering; corrosion resistance; mechanical properties

The high entropy alloys (HEAs) are multi-principal component alloys containing at least five elements with equiatomic or near-equiatomic content of 5at% ~35at% for each element^[1-3]. HEAs have excellent performance, such as good thermal stability, high strength, good wear resistance, and high hardness^[4-6], thereby attracting much attention in the defense, aerospace, and automobile industries as the structural materials.

Currently, many manufacturing techniques, such as arc melting, induction melting^[7,8], Bridgman solidification^[9], and powder metallurgy (PM)^[10,11], have been used to produce HEAs. Among them, PM is a typical bottom-up process, which can avoid or greatly reduce the metal removal process, thereby drastically reducing the production cost^[12]. The spark plasma sintering (SPS) is a novel PM method with fast heating and cooling rate and short holding time^[13]. The heating power mainly comes from the joule heating during the particle

contacts and the high energy spark plasma at the gaps between particles^[14]. Thus, SPS can achieve HEAs with high density, fine grains, and good mechanical properties. Kumar et al^[15] prepared the AlCuCrFeMnW HEAs via the mechanical alloying (MA) followed by SPS, and found that the HEA hardness reaches 8731.8 MPa. Pohan et al^[16] prepared the Al_{0.3}CoCrFeMnNi HEAs by SPS and observed that the compressive yield strength and compressive ductility are 979±20 MPa and 39%±3%, respectively. Ivchenko et al^[17] investigated the microstructure and nano-properties, such as hardness, elastic modulus, and creep resistance, of HEAs. However, the corrosion resistance and mechanical properties of individual phases in HEAs are rarely reported.

In this research, the AlCrCoFeNi_{2.1} HEAs were prepared by SPS at different sintering temperatures. The microstructure, corrosion resistance, and mechanical properties of the prepared HEAs were studied. The hardness and contact

Received date: November 26, 2021

Foundation item: National Natural Science Foundation of China (51805358, 51775366); Key Research and Development Program of Jinzhong (Y201023); College Students' Innovative Entrepreneurial Training Plan Program (202010112011)

Corresponding author: Chen Hongsheng, Ph. D., Associate Professor, College of Mechanical and Vehicle Engineering, Taiyuan University of Technology, Taiyuan 030024, P. R. China, Tel: 0086-351-6010076, E-mail: chen hongsheng@tyut.edu.cn

Copyright © 2022, Northwest Institute for Nonferrous Metal Research. Published by Science Press. All rights reserved.

modulus of individual phases in the biphase AlCrCoFeNi_{2,1} HEAs at different strain rates was studied. Besides, the corrosion, strengthening, and fracture mechanisms were discussed.

1 Experiment

The AlCrCoFeNi_{2,1} HEA powder was sintered by SPS through the SPS-331Lx equipment. The morphology and particle size distribution of the HEA powder are shown in Fig.1. The powder was placed in a graphite mold with 20 mm in diameter and SPS was conducted in vacuum at different temperatures (850, 950, 1050, and 1150 °C). In this study, the whole sintering process was conducted at pressure of 30 MPa under the holding time of 5 min. The vacuum degree and heating rate were about 10 Pa and 50 °C/min, respectively.

The relative density of the sintered specimens was measured by the Archimedes principle. The microstructures of sintered HEAs were observed by the optical microscope (OM) and the scanning electron microscope (SEM, JSM6700F) at second electron (SE) and backscattered electron (BSE) modes coupled with an electron backscattered diffraction (EBSD, Oxford Instrument) system. The phase evaluation of the AlCrCoFeNi_{2,1} HEA was investigated by the X-ray diffractometer (XRD, D/MAX2400, Cu K α). The energy disperse spectroscopy (EDS) was also used for analysis. The corrosion resistance of the AlCrCoFeNi_{2,1} HEA was evaluated by the potentiodynamic polarization (PDP) tests. The specimen with the surface area of 0.5 cm² was exposed to the 3.5wt% NaCl solution. After the PDP tests, the specimen surface was observed by SEM. The hardness of body-centered cubic (bcc) and face-centered cubic (fcc) phases was measured by the nanoindentation (Agilent G200), and the plastic deformation pile-up around the indentation edges was tested by the laser confocal microscopic (LCM). The tensile tests at strain rate of 0.2 mm/min and room temperature were conducted by DNS200 equipment and the fracture surface was observed. Each test was repeated 3 times to ensure consistency.

2 Results and Discussion

2.1 Microstructure

The relative density of the AlCrCoFeNi_{2,1} HEAs after SPS at different temperatures is shown in Table 1. The results show

that the relative density of HEAs is improved with increasing the sintering temperature. The relative density of HEA after SPS at 1150 °C can reach 99.18%, because the high sintering temperature leads to the fully thermoplastic deformation of alloy particles. In addition, the microvoids between the particles disappear, which also improves the relative density of the AlCrCoFeNi_{2,1} HEA. The maximum relative density of 99.18% is even higher than that of 98.23% of HEAs after SPS at 1150 °C in Ref.[18], due to the longer sintering time in this research.

OM microstructures of AlCrCoFeNi_{2,1} HEAs after SPS at different temperatures are shown in Fig.2. It can be seen that the surface of the specimen sintered at 850 °C has numerous voids and the bonding between particles is weak, which indicates that the low sintering temperature causes the insufficient sintering. With increasing the sintering temperature, the sintered specimens become denser and more compact. However, the micropores in the specimen sintered at 1150 °C increase slightly in number, compared with those in the specimens sintered at 950 and 1050 °C, as indicated by the red arrows in Fig. 2d. The electric current cannot homogeneously pass through the materials, leading to the high local current density and (over) heating^[19]. With increasing the sintering temperature, the local volatilization of the powder surface and the element burn loss may occur during SPS process due to the high local temperature at the sintering neck, therefore forming the micropores^[20]. It is known that with increasing the temperature, the bcc phase in AlCrCoFeNi_{2,1} HEA is gradually transformed into fcc phase which has a tight lattice binding^[21,22], therefore leading to the continuous increase of the relative density.

Fig.3 presents SEM-SE and SEM-BSE microstructures of AlCrCoFeNi_{2,1} HEAs after SPS at 1050 °C. The typical areas can be observed in HEA: the bright area indicated by the red arrows is fcc phase and the dark area indicated by the white arrows is bcc phase. It can be seen that the small bcc phase is relatively homogeneously distributed in the fcc phase. The interface between particles disappears and the bonding between the phases is good in AlCrCoFeNi_{2,1} HEA after SPS at 1050 °C.

Fig. 4 shows the phase map and phase size distributions of bcc and fcc phases in AlCrCoFeNi_{2,1} HEA after SPS at 1050 °C. The average phase sizes of bcc and fcc phases are

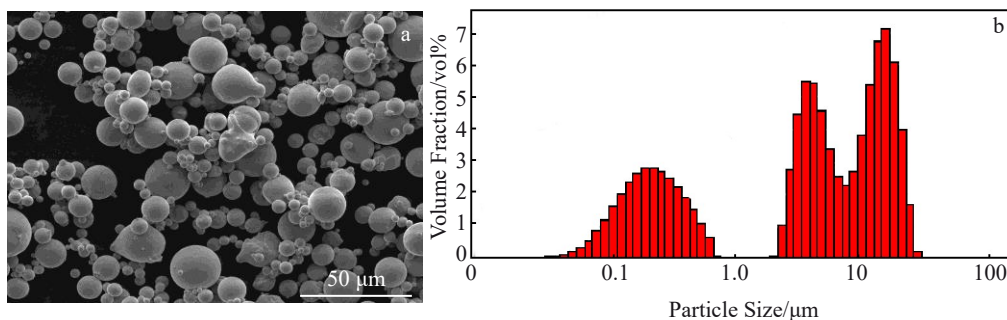


Fig.1 Morphology (a) and particle size distribution (b) of AlCrCoFeNi_{2,1} HEA powder

Table 1 Relative density of AlCrCoFeNi_{2,1} HEAs after SPS at different temperatures

Sintering temperature/°C	850	950	1050	1150
Relative density/%	93.25	97.32	98.93	99.18

1.46 and 3.41 μm , respectively. As shown in Fig. 4a, the sintered HEA is composed of fcc and bcc phases, and fcc phase is in the domination position. The phase fraction of fcc phase can be calculated by Eq.(1), as follows:

$$\text{Phase fraction of fcc phase} = \frac{I_{\text{fcc}}}{I_{\text{fcc}} + I_{\text{bcc}}} \times 100\% \quad (1)$$

where I_{fcc} and I_{bcc} are the relative areas of fcc and bcc phases in the phase map, respectively. Thus, the phase fraction of fcc and bcc phases is 79.4% and 20.6%, respectively.

Fig.5 shows SEM microstructure and EDS analysis results of AlCrCoFeNi_{2,1} HEA after SPS at 1050 °C. In Fig. 5a, the point A represents the bcc phase, point B represents the fcc phase, and point C represents the interface between the bcc and fcc phases. EDS analysis results of point A and B are shown in Fig.5b and 5c, respectively. It is found that the point A is rich in Al and Ni, while the point B is rich in Cr, Co, and Fe. The approximate chemical composition of fcc and bcc phases is Al₁₀Cr₂₂Co₁₈Fe₂₀Ni₃₂ and Al₂₇Cr₉Co_{12.7}Fe_{10.8}Ni_{40.5} (at%), respectively. Point C is located in the transition region. The EDS line scanning result along the yellow line in Fig.5e shows that the bcc phase is rich in Al and Ni, and fcc phase is rich in Cr, Co, and Fe. Fig. 6 shows the EDS element distributions of AlCrCoFeNi_{2,1} HEA after SPS at 1050 °C. The crystal structure of the bright area is the fcc phase containing a large amount of Cr, Co, and Fe; the crystal structure of the dark area is the bcc phase containing a large amount of Al and Ni. Hence, the AlCrCoFeNi_{2,1} HEA is a biphas (fcc and bcc solid solution) alloy.

Fig. 7 shows XRD patterns of the original AlCrCoFeNi_{2,1}

HEA powder and AlCrCoFeNi_{2,1} HEA specimen after SPS at 1050 °C. It is clear that after SPS at 1050 °C, the intensity of the fcc phase peak increases significantly and that of the bcc peak decreases, indicating the transformation from bcc phase to fcc phase during SPS process.

Fig.8 shows the recrystallized, substructured, and deformed structures in AlCrCoFeNi_{2,1} HEA after SPS at 1050 °C. Compared with those in fcc phase, the area fraction of recrystallized and deformed structures in bcc phase is higher in the AlCrCoFeNi_{2,1} HEA, which is about 81.48% and 7.78%, respectively. It is clear that the area fraction of substructure (44.29%) is higher in the fcc phase than that in the bcc phase (10.74%).

2.2 Corrosion resistance

The potentiodynamic polarization experiments were conducted in 3.5wt% NaCl solution to evaluate the electrochemical corrosion resistance of AlCrCoFeNi_{2,1} HEAs. PDP curves of AlCrCoFeNi_{2,1} HEAs after SPS at different temperatures are shown in Fig.9. Based on the line fitting by Tafel method, the corresponding corrosion potential (E_{corr}) and corrosion current density (i_{corr}) are obtained, as listed in Table 2. It is known that E_{corr} can describe the thermodynamical properties of materials, which indicates the general corrosion tendency. However, it cannot be used to evaluate the corrosion rate of specimens^[23-25]. Zhang et al^[26] also indicated that E_{corr} cannot be used as the main factor to evaluate corrosion resistance. Therefore, i_{corr} is commonly considered as the kinetic corrosion rate, which can evaluate the damage to material, as described by Eq.(2)^[27-30], as follows:

$$V_{\text{acr}} = \frac{3.27 \times 10^{-3} i_{\text{corr}} EW}{D} \quad (2)$$

where V_{acr} is the average corrosion rate of alloy ($\text{mm} \cdot \text{a}^{-1}$), EW is the equivalent mass of alloy, i_{corr} is the corrosion current density of alloy ($\mu\text{A} \cdot \text{cm}^{-2}$), and D is the density of alloy ($\text{g} \cdot \text{cm}^{-3}$). According to the Stern-Geary equation, the higher

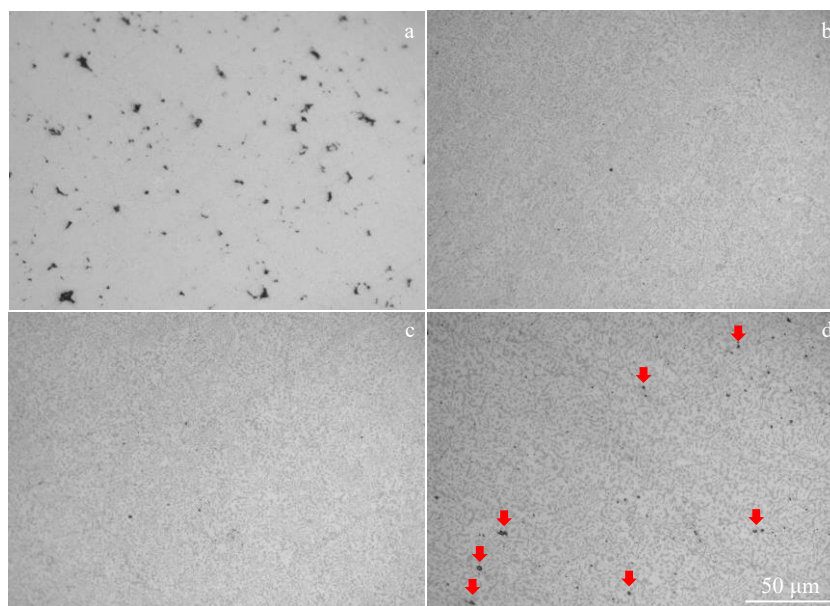


Fig.2 OM microstructures of AlCrCoFeNi_{2,1} HEAs after SPS at different temperatures: (a) 850 °C, (b) 950 °C, (c) 1050 °C, and (d) 1150 °C

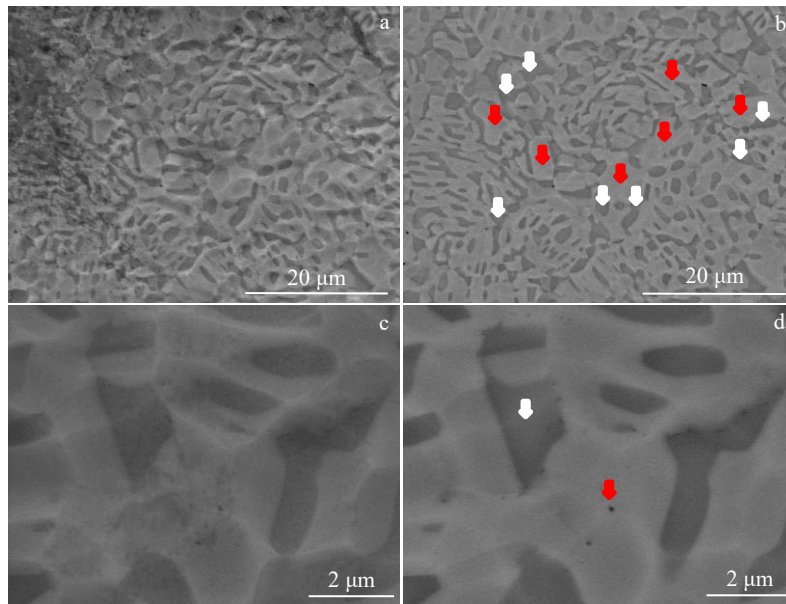


Fig.3 SEM-SE (a, c) and SEM-BSE (b, d) microstructures of AlCrCoFeNi_{2.1} HEAs after SPS at 1050 °C

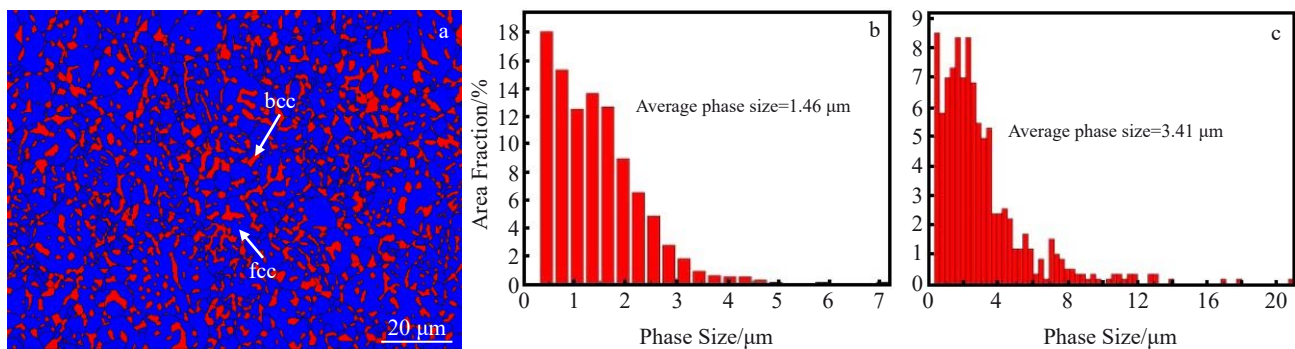


Fig.4 Phases map (a) and phase size distributions of bcc phase (b) and fcc phase (c) of AlCrCoFeNi_{2.1} HEA after SPS at 1050 °C

the i_{corr} , the lower the polarization resistance (R_p)^[31]. Therefore, i_{corr} is an important parameter to evaluate the corrosion resistance of AlCrCoFeNi_{2.1} HEA.

The HEA specimen sintered at 950 °C has the lowest i_{corr} and the relatively higher E_{corr} , demonstrating the better corrosion resistance. The i_{corr} of HEA specimen sintered at 1050 °C is slightly improved. The i_{corr} of HEA specimens sintered at 850 and 1150 °C is relatively high and has a small difference, demonstrating the faster corrosion rate. It is found that with increasing the sintering temperature or annealing temperature, the bcc phase is gradually transformed to fcc phase due to the Al concentration in the phases^[32-34]. The phase transformation can also be observed in Fig. 7. The fcc phase has tight lattice binding, which requires more energy for atom movement, i. e., the more the fcc phase, the better the corrosion resistance^[35]. The weak spots on the alloy surface (voids, pores, inclusions, intermetallics, mechanical flaws) can induce faster inward diffusion of Cl⁻ ions, resulting in the accelerated degradation^[30,36]. Therefore, the inferior corrosion resistance of AlCrCoFeNi_{2.1} HEA sintered at 850 °C is mainly

due to the existence of numerous voids (Fig.2a) and the high fraction of bcc phase. The enhanced corrosion resistance is obtained for HEAs sintered at 950 and 1050 °C, which may be attributed to the combined effects of few pores/voids, higher fraction of fcc phase, and higher relative density. Yao et al^[18] revealed that the number of intermetallic compounds, such as Al₃Cr₂, Al₁₃Co₄, and Al₉Co₄, in AlCrCoFeNi_{2.1} HEA sintered at 1150 °C is larger than that at 1050 °C. The galvanic corrosion can be formed between grains (cathode) and Al-rich particles (anode)^[37]. Therefore, the high corrosion rate of HEA sintered at 1150 °C is mainly attributed to the intermetallic compounds and some micropores (Fig.2d). The high E_{corr} of HEA sintered at 1150 °C may also be associated with the high fraction of fcc phase. In addition, with the electrochemical corrosion proceeding, more exposure of the intermetallic compounds and micropores may accelerate the corrosion rate.

Fig. 10 shows the corrosion morphologies of AlCrCoFeNi_{2.1} HEAs after SPS at 850 and 1150 °C and immersion in 3.5wt% NaCl solution at room temperature. As shown in Fig. 10, the corrosion is severe due to the poor corrosion resistance of

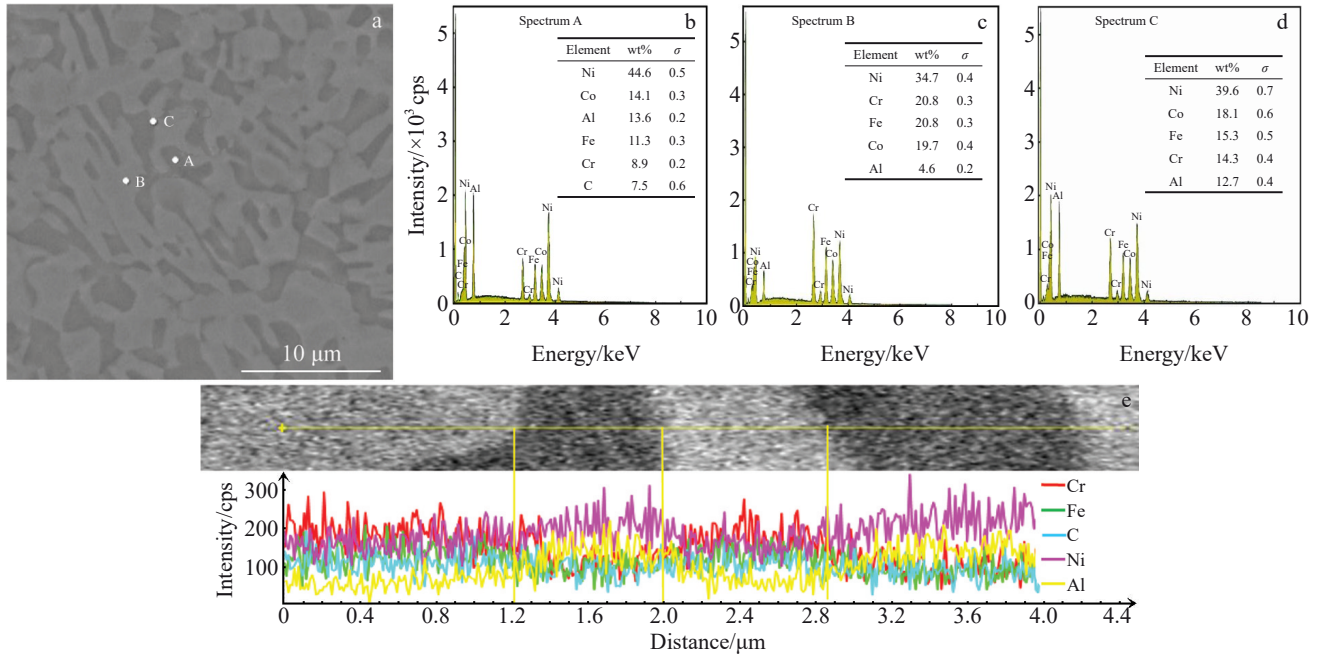


Fig.5 SEM microstructure of AlCrCoFeNi_{2.1} HEA after SPS at 1050 °C (a); EDS spectra of point A (b), point B (c), and point C (d) in Fig.5a; EDS line scanning results of AlCrCoFeNi_{2.1} HEA (e)

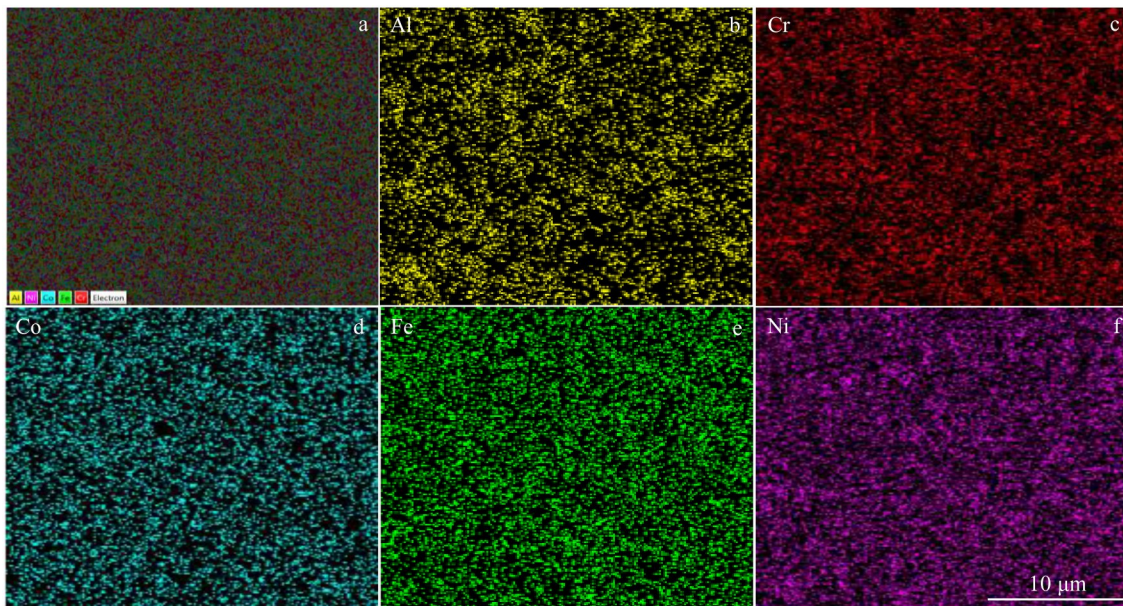


Fig.6 EDS element distributions of AlCrCoFeNi_{2.1} HEA after SPS at 1050 °C

HEA sintered at 850 °C, and only a few small corrosion pits occur on the surface of HEA sintered at 1050 °C due to its improved corrosion resistance. The small corrosion pits are gathered at the positions of bcc phase rather than those of the fcc phase, inferring the selective corrosion phenomenon. It is also proved that the bcc phase is preferentially attacked by the Cl⁻ ions^[38]. Sokkalingam^[37] and Li^[39] et al proposed the corrosion mechanism for Al_xCoCrFeNi (x=1, 0.5) HEAs: the localized pitting corrosion occurs due to the galvanic circuit between grain boundary (anode) and fcc islands (cathode), between grain boundary (anode) and grains (cathode) with

dissolution at grain boundaries, and between grains (cathode) and Al-rich particles (anode).

2.3 Mechanical properties

Fig. 11 shows the typical loading-unloading curves for the indentation tests on the fcc and bcc phases of AlCrCoFeNi_{2.1} HEAs sintered at 1050 °C at strain rates from 0.02 s⁻¹ to 0.5 s⁻¹. It can be seen that the load is increased with increasing the strain rate at the same displacement for the bcc and fcc phases. The pressure work and unloading work can be calculated by Eq.(3) and Eq.(4)^[40], respectively:

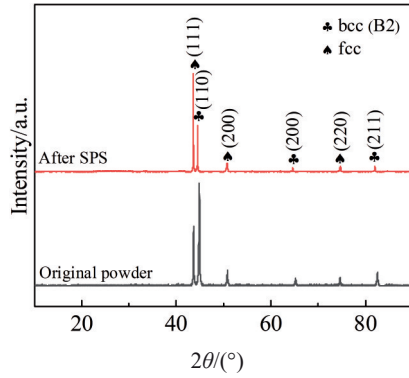


Fig.7 XRD patterns of AlCrCoFeNi_{2.1} HEA original powder and specimen after SPS at 1050 °C

$$w_t = \int_0^{h_m} Fdh \tag{3}$$

$$w_u = \int_{h_p}^{h_m} Fdh \tag{4}$$

where w_t and w_u are the pressure work and unloading work, respectively; h_m and h_p are the maximum depth and residual depth after unloading, respectively; F is the loading force; h is the depth. Based on Eq.(3) and Eq.(4), the pressure recovery rate can be calculated by Eq.(5), as follows:

$$\eta_{IT} = w_u/w_t \tag{5}$$

where η_{IT} is the pressure recovery rate. The calculated results are shown in Table 3. It is found that the η_{IT} is decreased and the hardening effect is enhanced with increasing the strain rate in the bcc and fcc phases. At the same strain rate, the η_{IT} in bcc phase is lower than that in fcc phase, which indicates that the

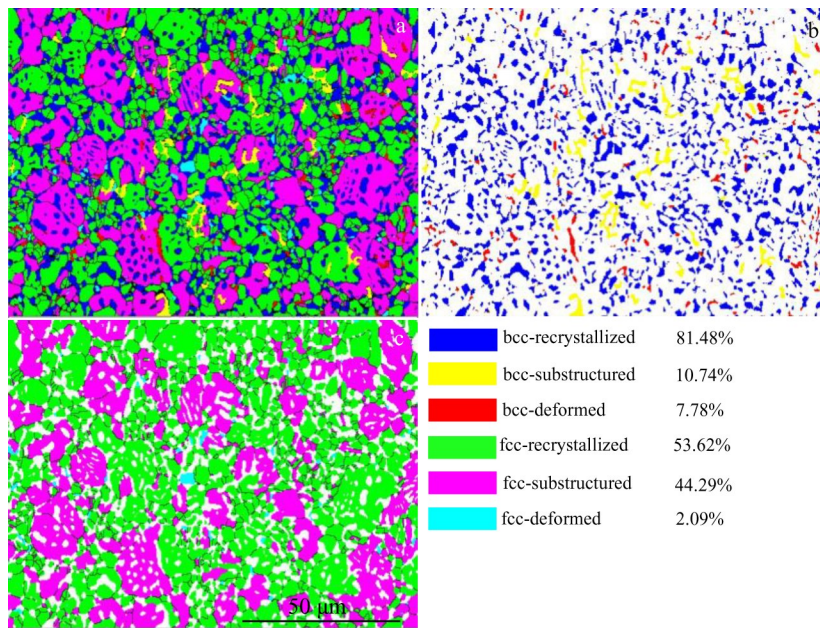


Fig.8 Recrystallized, substructured, and deformed structure distributions measured by EBSD in AlCrCoFeNi_{2.1} HEA after SPS at 1050 °C: (a) overall structure distribution; (b) in bcc phase; (c) in fcc phase

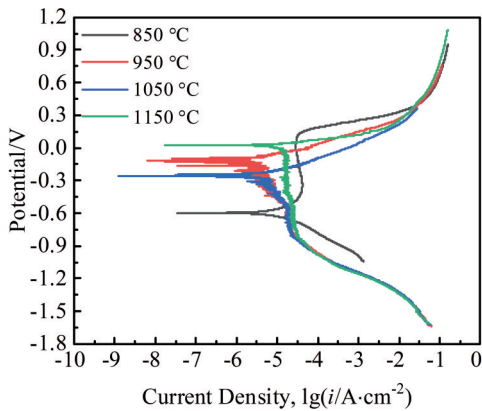


Fig.9 PDP curves of AlCrCoFeNi_{2.1} HEAs after SPS at different temperatures in 3.5wt% NaCl solution

Table 2 Corrosion potential E_{corr} and corrosion current density i_{corr} obtained by PDP curves of AlCrCoFeNi_{2.1} HEAs after SPS at different temperatures

SPS temperature/°C	Corrosion potential, E_{corr}/V	Corrosion current density, $i_{corr}/\mu A \cdot cm^{-2}$
850	-0.599	-4.875
950	-0.123	-5.410
1050	-0.267	-5.243
1150	-0.007	-4.821

plasticity of bcc phase is higher than that of fcc phase. As shown in Fig.11b and 11c, the nanohardness of fcc phase and the contact modulus of fcc and bcc phases in the AlCrCoFeNi_{2.1} HEA are firstly increased and then decreased

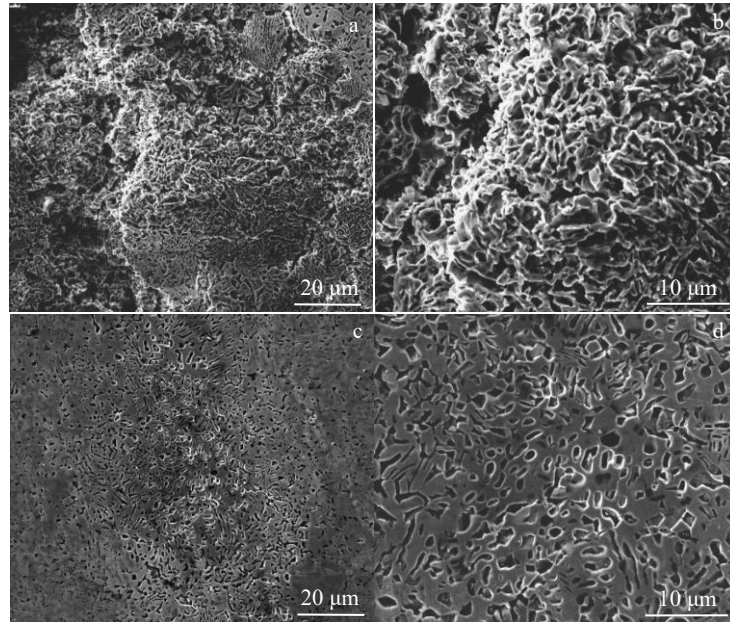


Fig.10 Corrosion morphologies of AlCrCoFeNi_{2.1} HEAs after SPS at 850 °C (a, b) and 1050 °C (c, d) and immersion in 3.5wt% NaCl solution at room temperature

with increasing the strain rate. The nanohardness of bcc phase is continuously increased with increasing the strain rate. Besides, the nanohardness and contact modulus of bcc phase at the same strain rate are higher than those of the fcc phase. The average nanohardness of the bcc and fcc phases is 6.25 and 4.09 GPa, respectively. The average contact modulus of

the bcc and fcc phases is 222.72 and 191.12 GPa, respectively. Fig. 11d shows the typical macroscopic morphology of the plastic deformation pile-up around the edges of indentation.

After the nanoindentation tests, the plastic deformation pile-up around the edges of indentations were obtained by LCM, as shown in Fig. 12. The depth profiles of the indentations and

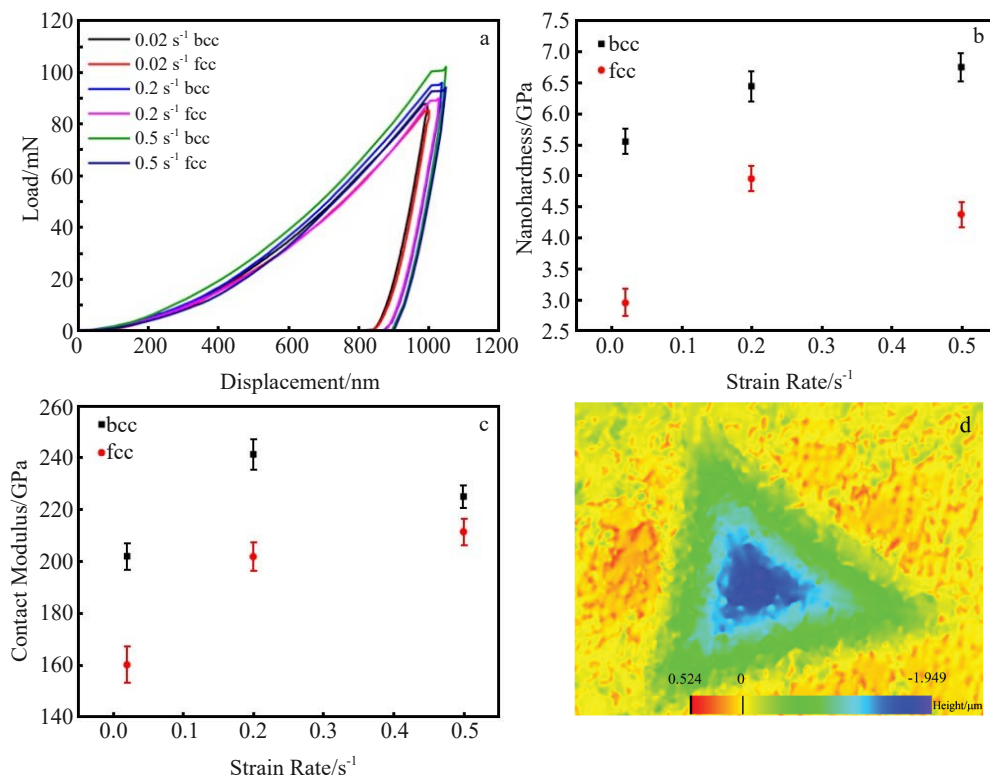


Fig.11 Relationships between load and displacement (a), nanohardness and strain rate (b), and contact modulus and strain rate (c) of AlCrCoFeNi_{2.1} HEAs sintered at 1050 °C; LCM morphology of plastic deformation pile-up around the edges of indentation (d)

Table 3 Parameters of w_p , w_u , and η_{IT} of AlCrCoFeNi_{2.1} HEAs at different strain rates

Parameter	bcc phase			fcc phase		
	0.02 s ⁻¹	0.2 s ⁻¹	0.5 s ⁻¹	0.02 s ⁻¹	0.2 s ⁻¹	0.5 s ⁻¹
$w_p/\times 10^{-9}$ J	31.18	36.14	39.84	29.60	32.13	35.03
$w_u/\times 10^{-9}$ J	5.30	5.87	5.87	5.10	5.32	5.50
$\eta_{IT}/\%$	17.00	16.24	14.73	17.23	16.58	15.70

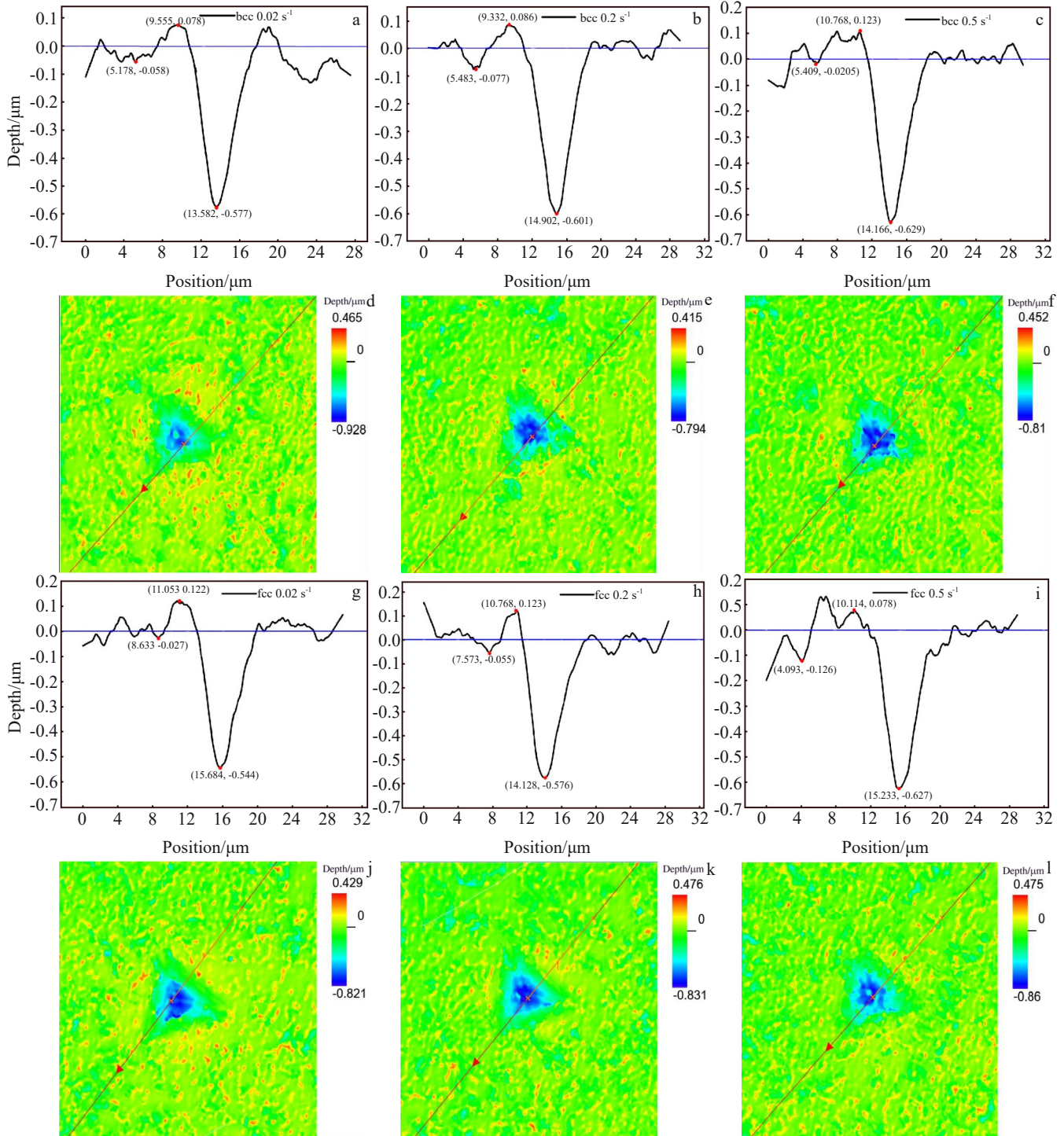


Fig.12 Depth profiles (a~c, g~i) and LCM images (d~f, j~l) of AlCrCoFeNi_{2.1} HEAs sintered at 1050 °C under different strain rates: (a, d) bcc-0.02 s⁻¹; (b, e) bcc-0.2 s⁻¹; (c, f) bcc-0.5 s⁻¹; (g, j) fcc-0.02 s⁻¹; (h, k) fcc-0.2 s⁻¹; (i, l) fcc-0.5 s⁻¹

LCM images of the nanoindentation at the surface edge of the indents of AlCrCoFeNi_{2.1} HEAs sintered at 1050 °C are also shown in Fig. 12. The average pile-up height h_p around the nanoindentations in fcc and bcc phases is 0.544~0.629 μm and the edge uplift height is 0.078~0.123 μm .

Fig. 13 displays the uniaxial tensile stress-strain curves of the AlCrCoFeNi_{2.1} HEAs after SPS at different temperatures. The yield strength (YS), ultimate tensile strength (UTS), elongation, and absorbed energy (AE) are all presented in Fig. 13. It is found that with increasing the SPS temperature, UTS, elongation, and AE of the AlCrCoFeNi_{2.1} HEAs are firstly increased and then decreased. The maximum UTS is 916.1 MPa, and YS and the elongation can reach 403 MPa and 14.87%, respectively. The mechanical properties of the HEA sintered at 850 °C are inferior due to the existence of numerous voids. It can be observed that with further increasing the sintering temperature from 1050 °C to 1150 °C, UTS and elongation of the AlCrCoFeNi_{2.1} HEAs are decreased, while YS is increased. Yao et al.^[18] reported that when the sintering temperature is above 1150 °C, the high sintering temperature can easily lead to the volatilization of Al and Ni elements and the coarsening of grains, which results in the reduction of hardness and compressive strength of AlCrCoFeNi_{2.1} HEAs. It is also reported that the number of intermetallic compounds in HEA sintered at 1150 °C is larger than that at 1050 °C. Therefore, the increase in YS of HEA sintered at 1150 °C may be due to the existence of intermetallic compounds which inhibit the dislocation movement. The coarsening of grains, a few micropores, and the plastic deformation mismatch between the intermetallic compounds and matrix may lead to the reduction in elongation of the HEA sintered at 1150 °C. The higher UTS of AlCrCoFeNi_{2.1} HEA sintered at 1050 °C may be attributed to the following factors.

(1) Grain size strengthening

The grain size strengthening (σ_{gss}) due to the fcc phase can be calculated by the Hall-Petch relationship^[41], as follows:

$$\sigma_{\text{fcc}} = \sum_{i=1}^5 \sigma_{0,i} C_{i,\text{fcc}} + \sum_{i=1}^5 k_i C_{i,\text{fcc}} d^{-1/2} \quad (6)$$

where $C_{i,\text{fcc}}$ represents the composition of i element in fcc

phase; d is the phase size; $\sigma_{0,i}$ and k_i are Hall-Petch coefficients of i element, as listed in Table 4^[40]. Based on the phase fractions of fcc and bcc phases in AlCrCoFeNi_{2.1} HEAs, the grain size strengthening in the AlCrCoFeNi_{2.1} HEA can be calculated by Eq.(7), as follows:

$$\sigma_{\text{gss}} = \sum_{p=1}^n \sigma_p X_p \quad (7)$$

where σ_p is stress of p phase and X_p is the phase fraction of p phase. Therefore, the σ_{gss} for AlCrCoFeNi_{2.1} HEA is about 77.5 MPa.

(2) Solid solution strengthening

The solid solution strengthening (σ_{sss}) caused by the increase in YS can be calculated by Eq.(8)^[42], as follows:

$$\sigma_{\text{sss}} = \frac{3.1\varepsilon G \sum_{i=1}^5 C_i^{1/2}}{700} \quad (8)$$

where G is the shear modulus of HEAs, ε is the lattice strain of the phase, and C_i is the fraction of i element in the phase. According to the calculation, σ_{sss} is 31.4 MPa. Therefore, the total contribution of grain size strengthening and solid solution strengthening on strength is 108.9 MPa. In addition, the good interface bonding between particles can improve the strength due to the load transfer effect.

During SPS process, the plasma can break the oxide layer and purify and activate the particles in HEAs. Under the pressure and joule heating, the gaps between the particles are decreased due to the tip discharge and the increased plasma effect. The high local temperature zone forms, resulting in the melting of the HEA particles. The simulation result is shown in Fig. 14a. Firstly, the vaporization and solidification occur. Subsequently, the surface diffusion occurs under the pressure and electric field. The discharge and plasma between the adjacent HEA particles stop when the connection between HEA particles is built. The neck is formed between HEA particles, and the microstructure of the sintering neck is shown in Fig. 14b. The schematic diagram of the neck formation is shown in Fig. 14c.

Fig. 15 shows SEM fracture morphologies of the AlCrCoFeNi_{2.1} HEA after SPS at 1050 °C. The fracture surface shows a lot of small dimples. As shown in Fig. 15b, the brittle fracture of bcc phase can be clearly observed. During the deformation process, the fcc phase is plastically deformed and the load is transferred to the hard brittle bcc phase. Once the stress concentration exceeds the fracture strength of HEAs, the bcc phase fractures. Therefore, the fracture mechanisms include the brittle fracture of bcc phase and the

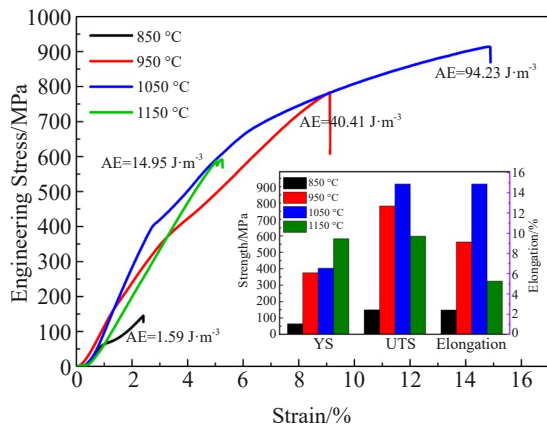


Fig.13 Engineering stress-strain curves and mechanical properties of AlCrCoFeNi_{2.1} HEAs after SPS at different temperatures

Table 4 Hall-Petch coefficient σ_0 and k of different elements in HEAs^[40]

Element	σ_0/MPa	$k/\text{MPa}\cdot\text{m}^{1/2}$
Al	16.0	0.07
Cr	454.0	0.95
Co	10.3	0.08
Fe	100.0	0.60
Ni	22.0	0.16

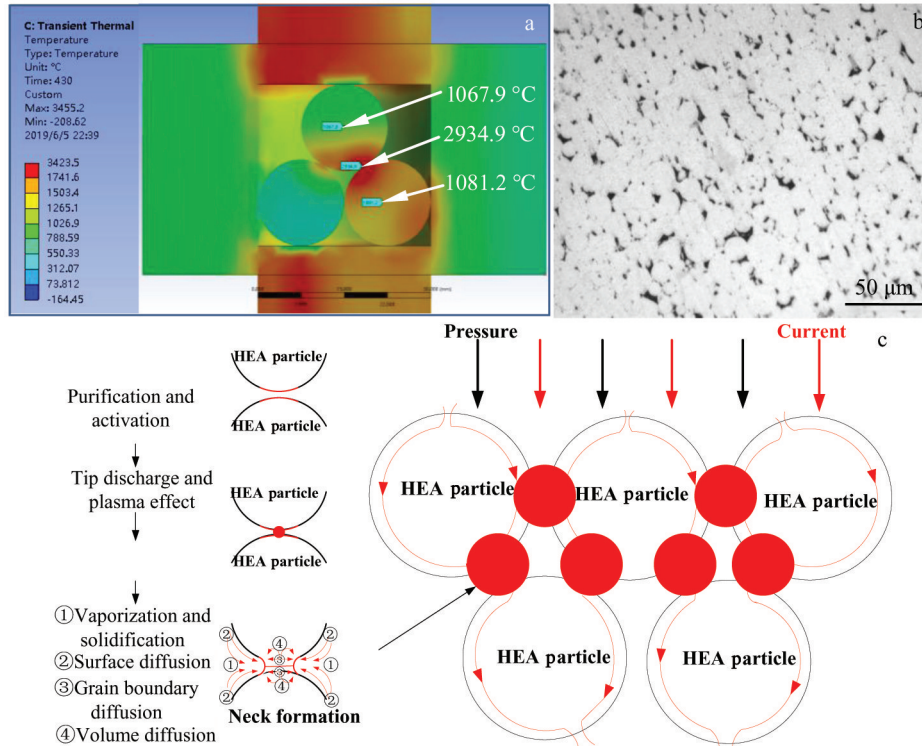


Fig.14 Simulation result of neck formation between HEA particles (a); microstructure of sintering neck at lower pressure (b); schematic diagram of neck formation (c)

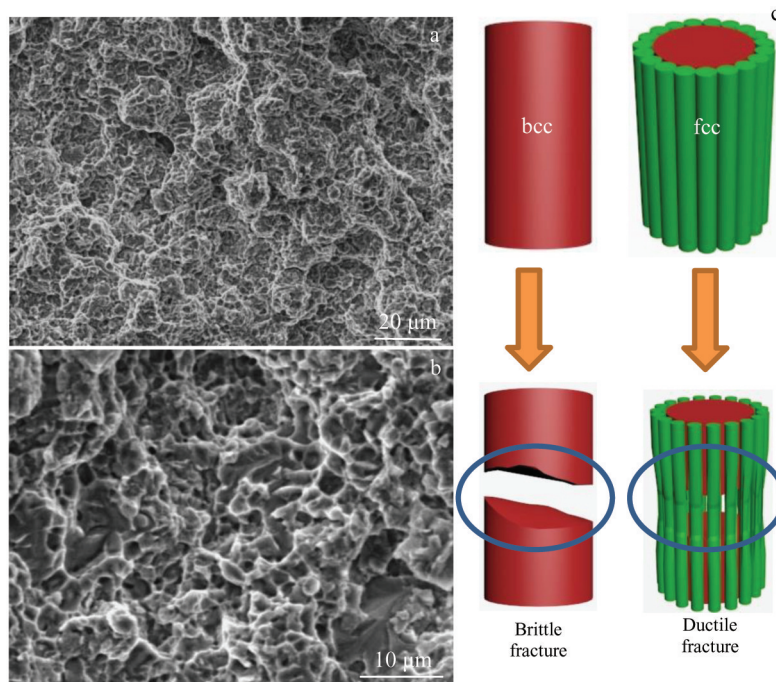


Fig.15 SEM fracture morphologies of AlCrCoFeNi_{2.1} HEAs after SPS at 1050 °C (a, b); schematic diagram of fracture mechanisms of bcc phase and fcc phase (c)

ductile fracture of fcc phase, as shown in Fig.15c.

3 Conclusions

1) During the spark plasma sintering (SPS) process, the

elements are relatively homogeneously distributed in the AlCrCoFeNi_{2.1} high entropy alloys (HEAs). The AlCrCoFeNi_{2.1} HEA is mainly composed of body-centered cubic (bcc) phase Al₂₇Cr₉Co_{12.7}Fe_{10.8}Ni_{40.5} and face-centered

cubic (fcc) phase $Al_{10}Cr_{22}Co_{18}Fe_{20}Ni_{32}$.

2) The pressure recovery rate (η_{IT}) is decreased and the hardening effect is enhanced with increasing the strain rate in the bcc and fcc phases. The hardness of the bcc phase is larger than that of the fcc phase.

3) The AlCrCoFeNi_{2,1} HEA sintered at 950 °C has the optimal corrosion resistance. The bcc phase can be easily corroded, compared with the fcc phase.

4) During the SPS process, the highest ultimate tensile strength is achieved for the HEA sintered at 1050 °C, because of the synergistic effects of the grain size strengthening, solid solution strengthening, and good interface bonding between the HEAs particles. The fracture mechanism is dominated by brittle fracture of bcc phase and ductile fracture of fcc phase.

References

- Singh A K, Anandh S. *Journal of Alloys and Compounds*[J], 2014, 587: 113
- Zhu Dezhi, Wu Jipeng, Liu Shiwen. *Rare Metal Materials and Engineering*[J], 2020, 49(11): 3875
- Jiang Shuying, Lin Zhifeng, Sun Yongxing. *Rare Metal Materials and Engineering*[J], 2018, 47(10): 3191 (in Chinese)
- Tang Z, Yuan T, Tsai C W et al. *Acta Materialia*[J], 2015, 99: 247
- Chen Z, Chen W P, Wu B Y et al. *Materials Science and Engineering A*[J], 2015, 648: 217
- Fu Z Q, Chen W P, Wen H M et al. *Journal of Alloys and Compounds*[J], 2015, 646: 175
- Bhattacharjee P P, Sathiaraj G D, Zaid M et al. *Journal of Alloys and Compounds*[J], 2014, 587: 544
- Zhang Jinyong, Wu Yijin, Zhao Congcong et al. *Rare Metal Materials and Engineering*[J], 2021, 50(11): 4135 (in Chinese)
- Shun T T, Du Y C. *Journal of Alloys and Compounds*[J], 2009, 478(1-2): 269
- Fan Yuhu, Zhang Yunpeng, Guan Hongyan et al. *Rare Metal Materials and Engineering*[J], 2013, 42(6): 1127
- Waseem O A, Lee J, Lee H M et al. *Materials Chemistry and Physics*[J], 2018, 210: 87
- Joo S H, Kato H, Jang M J et al. *Journal of Alloys and Compounds*[J], 2017, 698: 591
- Chen H S, Wang W X, Nie H H et al. *Vacuum*[J], 2017, 143: 363
- Zhang Z H, Liu Z F, Lu J F et al. *Scripta Materialia*[J], 2014, 81: 56
- Kumar D, Maulik O, Kumar S et al. *Materials Chemistry and Physics*[J], 2018, 210: 71
- Pohan R M, Gwalani B, Lee J et al. *Materials Chemistry and Physics*[J], 2018, 210: 62
- Ivchenko M V, Pushin V G, Uksusnikov A N et al. *Physics of Metals and Metallography*[J], 2013, 114(6): 503
- Yao Ruiming, Zheng Liuwei. *Materials for Mechanical Engineering*[J], 2019, 43(7): 28 (in Chinese)
- Zhou P F, Xiao D H, Wu Z et al. *Materials Research Express*[J], 2019, 6(8): 0865e7
- Guillon O, Gonzalez-Julian J, Dargatz B et al. *Advanced Engineering Materials*[J], 2014, 16(7): 830
- John R, Karati A, Joseph J et al. *Journal of Alloys and Compounds*[J], 2020, 835: 155 424
- Wang W R, Wang W L, Yeh J W. *Journal of Alloys and Compounds*[J], 2014, 589: 143
- Derakhshi M A, Kangazian J, Shamanian M. *Vacuum*[J], 2019, 161: 371
- Niu H Y, Deng K K, Nie K B et al. *Journal of Alloys and Compounds*[J], 2019, 787: 1290
- Luo W Y, Liu Y Z, Dong B W et al. *Intermetallics*[J], 2022, 151: 107 738
- Zhang C L, Zhang F, Song L et al. *Journal of Alloys and Compounds*[J], 2017, 728: 815
- Peng J H, Zhang Z, Long C et al. *Journal of Alloys and Compounds*[J], 2020, 827: 154 096
- Raphel A, Kumaran S, Kumar K V et al. *Materials Today: Proceedings*[J], 2017, 4(2): 195
- Chen Y Y, Duval T, Hung U D et al. *Corrosion Science*[J], 2005, 47(9): 2257
- Garip Y, Ergin N, Ozdemir O. *Journal of Alloys and Compounds* [J], 2021, 877: 160 180
- Brytan Z, Niagaj J, Reiman L. *Applied Surface Science*[J], 2016, 388: 160
- Zhou P F, Xiao D H, Yuan T C. *Acta Metallurgica Sinica (English Letters)*[J], 2020, 33(7): 937
- Munitz A, Salhov S, Hayun S et al. *Journal of Alloys and Compounds*[J], 2016, 683: 221
- Tsai M H, Yeh J W. *Materials Research Letters*[J], 2014, 2(3): 107
- Abhinav P, Mayur V, Nitish K et al. *Journal of Alloys and Compounds*[J], 2021, 863: 158 056
- Zhao R F, Ren B, Cai B et al. *Results in Physics*[J], 2019, 15: 102 667
- Sokkalingam R, Sivaprasad K, Duraiselvam M et al. *Journal of Alloys and Compounds*[J], 2020, 817: 153 163
- Wang S, Zhao Y H, Xu X T et al. *Materials Chemistry and Physics*[J], 2020, 244: 122 700
- Li Q H, Yue T M, Guo Z N et al. *Metallurgical and Materials Transactions A*[J], 2013, 44(4): 1767
- Sun Y, Zhao G F, Wen X Y et al. *Journal of Alloys and Compounds*[J], 2014, 608: 49
- Sriharitha R, Murty B S, Kottada R S. *Journal of Alloys and Compounds*[J], 2014, 583: 419
- Maulik O, Kumar D, Kumar S et al. *Intermetallics*[J], 2016, 77: 46

放电等离子烧结双相 AlCrCoFeNi_{2.1} 高熵合金的微观组织、 耐腐蚀性能和力学性能

郑凡林¹, 孙天鸣³, 池涵娟², 陈洪胜^{1,4}, 王文先^{3,4}

(1. 太原理工大学 机械与运载工程学院, 太原 山西 030024)

(2. 太原六味斋实业有限公司, 太原 山西 030006)

(3. 太原理工大学 材料科学与工程学院, 太原 山西 030024)

(4. 先进镁基材料山西省重点实验室, 太原 山西 030024)

摘要: 采用放电等离子烧结法在不同温度下制备 AlCrCoFeNi_{2.1} 高熵合金 (HEA), 并对其微观组织、耐腐蚀性能和力学性能进行了研究。结果表明, 烧结后的 AlCrCoFeNi_{2.1} HEA 最大相对密度可达 99.18%; 该 HEA 主要由体心立方 (bcc) 相和面心立方 (fcc) 相组成, 其比例分别为 20.6% 和 79.4%。与 fcc 相相比, AlCrCoFeNi_{2.1} HEA 中 bcc 相的再结晶组织和变形组织更多, 且 bcc 相在 3.5% (质量分数) NaCl 溶液中更容易被腐蚀。随着应变速率的增加, bcc 相和 fcc 相的压力恢复速率降低, 硬化效果增强。在 1050 °C 下烧结的 AlCrCoFeNi_{2.1} HEA 具有较高的极限抗拉伸强度, 这主要归因于晶界强化、固溶强化和合金粒子之间良好的界面结合。该 HEA 的断裂形式包括 bcc 相的脆性断裂和 fcc 相的韧性断裂。

关键词: 高熵合金; 放电等离子烧结; 耐腐蚀性能; 力学性能

作者简介: 郑凡林, 男, 1996 年生, 硕士生, 太原理工大学机械与运载工程学院, 山西 太原 030024, 电话: 0351-6010076, E-mail: 1261455309@qq.com